Classification of in-situ Solar Wind Data Measured by Solar Orbiter/SWA-PAS and HIS using Machine Learning

 $\begin{array}{c} \text{Liang Zhao lzh@umich.edu}^{1[0000-0002-5975-7476]}, \ \text{Henry} \\ \text{Han}^{2[0000-0003-0273-6719]} \ \text{henry_han@baylor.edu}, \ \text{Susan T. Lepri} \\ \text{slepri@umich.edu}^{1[XXXXX]}, \ \text{and} \ \text{Ryan Dewey rmdewev@umich.edu}^{1[XXXX]} \end{array}$

- Department of Climate and Space Sciences and Engineering, University of Michigan, Ann Arbor, MI 48109, USA
- ² Department of Computer Science, School of Engineering and Computer Science, Baylor University, Waco, TX 76798 USA

Abstract. Connecting in-situ solar wind properties with their source regions on the Sun has long been one of the unsolved questions in heliophysics. This challenge can now be addressed using modern AI/ML techniques and big data analysis algorithms. In this work, we apply state-of-the-art AI/ML technology on in-situ solar wind measurements made by the Heavy Ion Sensor (HIS) and Proton and Alpha Particle Sensor (PAS) onboard the recent Solar Orbiter mission (launched in 2020) to classify different types of solar wind. These data-driven classifications may provide insights into their coronal origins and could significantly help heliophysicists in understanding the long-standing question of where the slow solar wind originates.

Keywords: Solar wind \cdot Classification \cdot Machine Learning \cdot Heliophysics

1 Introduction

Solar wind is crucial to space weather science and forecasting because the properties of the solar wind plasma affect the local conditions in the entire Heliosphere, and largely determine the propagation, arrival time and geo-effectiveness of solar eruptions. In addition, solar wind plasma is inextricably tied to the thermal properties of the inner corona where it is accelerated, heated, and ionized. For example, coronal holes (CHs), where the fast wind is accelerated from, are regions where the plasma electron density and temperature are lower than in their surroundings, and consequently the wind originating from CHs is usually characterized by overall lower plasma ionization and heavy ion charge state ratios (e.g., O^{7+}/O^{6+} or C^{6+}/C^{5+}) [1]. Figure 1 shows polar plots of Ulysses'first (18 June 1993–10 January 1997) and third orbit (30 October 2005–30 June 2009) observations during solar minima: fast and less ionized wind was dominant in high latitude regions where polar CHs were prevalent.

On the contrary, no such direct connection can be found between the slowspeed solar wind and a specific source region in the Sun: the slow solar wind

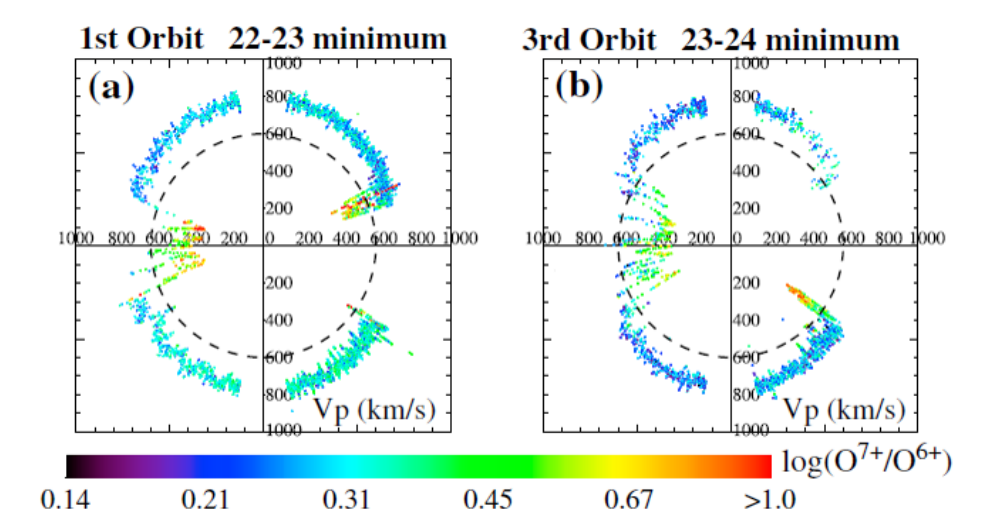


Fig. 1. Polar plots of solar wind proton speed (color coded with O^{7+}/O^{6+} ratio) from Ulysses' first (a) and third (b) orbits. Time goes in clockwise direction, starting from the bottom right quadrants. Figure adapted from [16]

might be originating from anywhere outside polar CHs, and even from their edges. Figure 1 shows that in the low latitude regions the solar wind speed are mostly slow or intermediate and the ionization level (indicated by O^{7+}/O^{6+} ratio) is higher than in the fast wind. The sources of these slow and hot wind has been variously suggested to be multiple types of coronal regions, including the periphery of active regions (ARs, e.g., [2, 3]), helmet streamers [4, 5, 7], CH boundaries [8], or pseudostreamers [10]. The latter structure consists of two sets of closed magnetic loops that separate open flux with the same polarity [12, 13], and they were abundant between 2007 and 2009 [14,15]. The solar wind originating from pseudostreamer regions has been suggested to have slow to intermediate speeds and to be highly ionized (high O^{7+}/O^{6+} ratio, [16]). Besides these origins, the slow-speed wind can also come from low-latitude CHs. For example, slow solar wind (V<600 km/s) observed by ACE around the ecliptic plane has been associated with low-latitude CHs because its variability, composition, and properties are very similar to CH-associated fast wind [4,7]. Now the question is, besides the clear association between the fast wind and polar CHs, the solar origins of the low to intermediate speed wind still remain a puzzle.

To solve this puzzle, solar wind heavy ion composition measurements are the the key factor that we need to rely on to link the solar wind from the heliosphere to its solar sources. The important role that the heavy ion charge state and element abundance play in understanding the solar wind and the heliosphere is twofold. First, they are unique tools to connect the in-situ solar wind properties to their origins in the corona. As the solar wind is accelerated, the plasma ionization and recombination rates are proportional to the electron

density, which rapidly decreases with distance. At a critical height where the electron density is so low that the two processes effectively stop [1] and the ionization state of an element remains unaltered as the solar wind propagates into the heliosphere (so-called "freeze-in" process, Figure 2); hence solar wind ion composition provides a direct measure of the thermal properties in the corona [4, 5, 17, 18]. In addition, element abundance ratios can be affected by fractionation processes in the upper chromosphere resulting in a significant enhancement of the abundance of elements with low First Ionization Potential (FIP < 10 eV) in closed magnetic, field structures over their values in photosphere [19–21, 7]. This is the so-called FIP effect (Figure 3, [31]). Such fractionation is directly inherited by the wind plasma and once the wind plasma is accelerated away, the abundance values remain unaltered and thus maintain record of the composition of the source region (e.g., [22]).

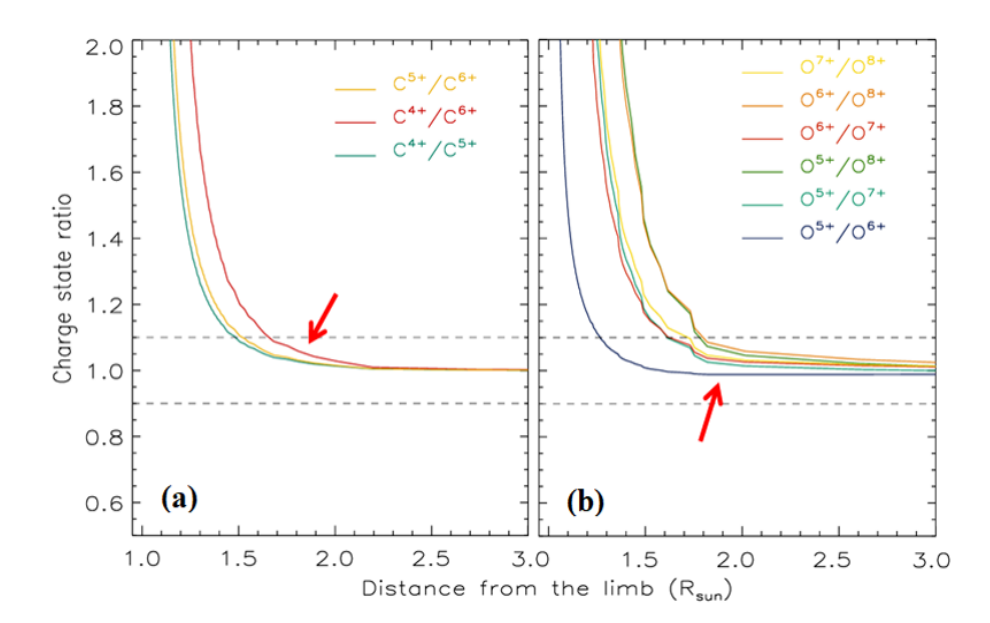


Fig. 2. Evolution of charge state ratios of Carbon (a) and Oxygen (b) as a function of distance from the solar limb (at 1 R_s) calculated by an Ionization model [23]. Red arrows point to where the charge states of C and O are frozen-in. Figure adapted from [23]

Second, in-situ anomalous composition data are tightly linked to the process of CME eruptions and can yield important insights into the characteristics of the CME source environment. [24] presented the first systematic search for hot material inside ICMEs observed by ACE/SWICS and found that more than 50% of ICMEs exhibited long periods (>20 hrs) of enhanced ${\rm Fe}^{>16+}/{\rm Fe}_{total}$ (Figure 4). Later work by Gruesbeck et al. (2011) showed that elevated Fe charge

4

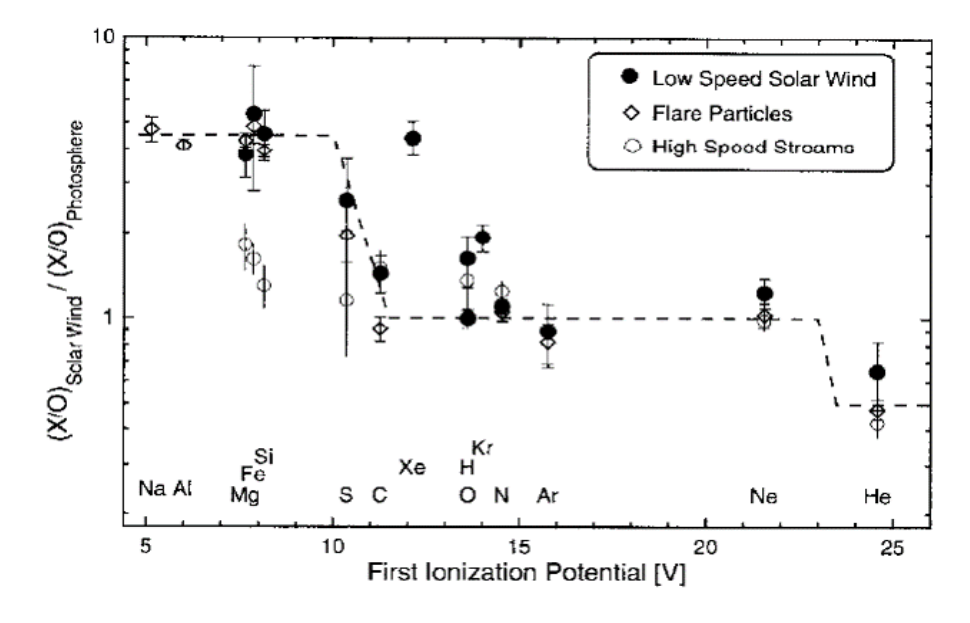


Fig. 3. Elemental abundances as a function of FIP in the slow wind and fast wind. Abundances are given relative to O and normalized to the photosphere abundances (Anders and Grevesse, 1989). Figure adapted from [19]

states are actually present in more than 95% of ICMEs. These elevated charge states (C, O, Si, Fe) indicate enhanced electron densities and temperatures most likely linked to plasma heating due to the deposition of magnetic energy during reconnection. [25] also reported a number of events where unusually cold material (Fe⁴⁻⁷⁺, O²⁻⁴⁺, C²⁻³⁺) was also present in in-situ measurements of ICMEs; this indicates the presence of low electron temperatures in the source region, likely related to prominence material. Motivation to the proposed research: The heavy ion composition data are valuable diagnostic tools that can be utilized to link the wind plasma parcels with specific structures in the inner corona where the wind origins and to characterized the solar origins and the properties of ICMEs.

Since solar wind heavy ions play a crucial role as significant test particles and respond uniquely to the heliospheric environment surrounding them, understanding the properties of the solar wind heavy ions composition is imperative for tracing heliospheric structures to their sources on the Sun or local sources in interplanetary space. The Solar Orbiter mission [26] is equipped with a Solar Wind Analyser (SWA, [27]), comprising the Proton and Alpha Particle Sensor (PAS) and the Heavy Ion Sensor (HIS, [28]). The integration of these new instruments opens a new era of modern solar wind heavy ion in-situ observations, succeeding the pioneering missions of Ulysses and ACE. Now we have a unique opportunity to fully harness the scientific potential of solar wind composition measurements by Solar Orbiter, allowing us to gain deeper insights into our understanding of the inner heliosphere and beyond.

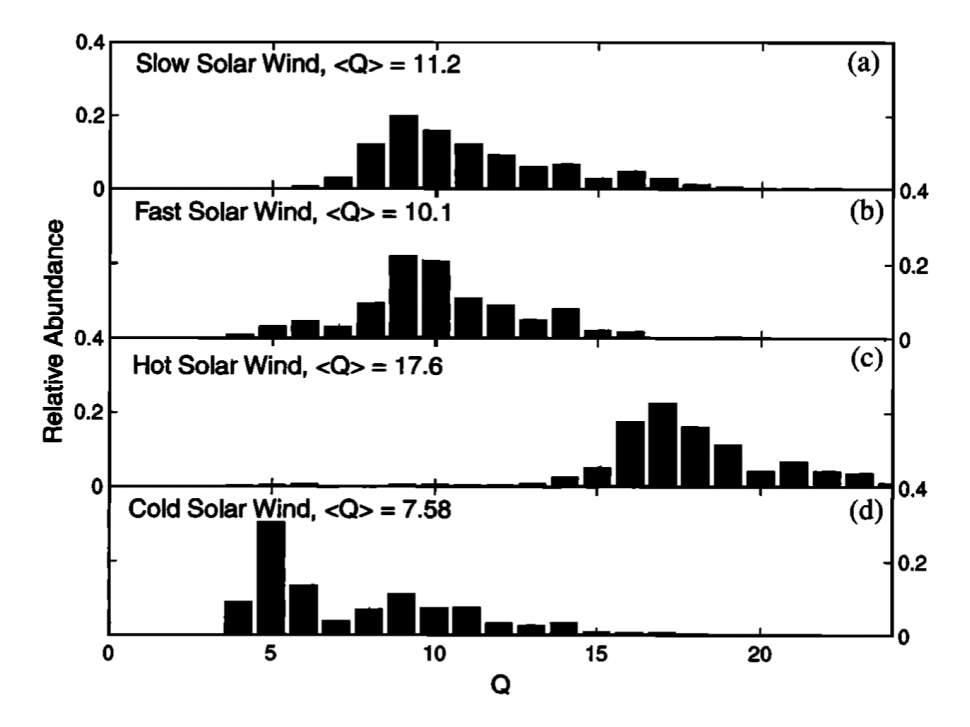


Fig. 4. Examples of Fe charge state distributions. (a) A distribution for typical slow solar wind with an average charge state corresponding to a coronal collisional equilibrium electron temperature of T=1.4 MK (0000-0200 UT, September 7, day 250, 1998). (b) A distribution for fast solar wind with a corresponding temperature of T=1.2 MK (0000-0200 UT, July 24, day 205, 1998). (c) A distribution for hot solar wind corresponding to coronal collisional equilibrium electron T= 7.3 MK (2000-2300 UT, September 25, day 268, 1998). (d) A cold solar wind charge distribution with T=0.6 MK (000-0200 UT, September 25, day 268, 1998). Note that the distributions in Figures 1b and 1c were obtained on the same day. Figure adapted from [24]

It is the purpose of this paper to apply Machine Learning clustering algorithms on the recent Solar Orbiter observations during 2022, in order to category the data into multiple clusters and then to understand the differences between these clusters in terms of their in-situ physical properties, and their possible difference in the coronal origins. In section 2, we introduce the Solar Orbiter data we use in this work. Section 3 describes the ML feature selection process that we apply on the solar orbiter data. In section 4, we discuss the ML clustering procedure and present the clustering results. In section 5, we investigate the differences in the in-situ properties of these different clusters of solar wind as identified by the ML algorithm, and discuss the implications for their coronal origins. Finally, in section 6, we summarize our results, discuss the significance of this work, and outline future plans.

2 Solar Orbiter Observations

With the launch of Solar Orbiter in 2020 [26], new measurements of solar wind, including heavy ion properties, are now available in the inner heliosphere. These measurements, from the Solar Wind Analyzer (SWA, [27]) allow us to extender our previous analysis (e.g., [4, 5, 5] into the most recent solar cycle. In particularly, the SWA suite is comprised of the Proton and Alpha Sensor (PAS), the Electron and Alpha Sensor (EAS-double check acronym) and the Heavy Ion Sensor (HIS, [28]), and provides the opportunity to investigate the properties of the slow-speed solar wind from 2022, close to the solar maximum of cycle 25.

The in-situ solar wind measurements we used in the work as input for the ML clustering models are: 10-minute resolution of ${\rm O^{6+}/O^{4+}}$, ${\rm O^{6+}/O^{4+}}$, ${\rm C^{6+}/C^{5+}}$, abundance ratio Fe/O, and average charge state of Oxygen, from Solar Orbiter/HIS, during Jan. 2022 to Apr. of 2024. And proton speed and density data as measured by Solar Orbiter/PAS, averaged into the 10-minute winder to match with HIS data.

3 Feature Selection to Rank the Importance of the Solar Wind Parameters of Solar Orbiter Observation

Feature selection is a crucial process in ML/AI data analysis. The goal of this procedure is to rank the input features (variables) by their importance, so that to enhance the interpretability of the data, decrease computational complexity, improve model performance, and reduce possible overfitting. In this study, we apply ML feature selection on the Solar Orbiter/PAS and HIS measurements during 2022. By discerning which variables are essential, we build an interpretable and efficient ML/AI system by exploiting the most influential variables. In Figure 5 we utilized extremely randomized trees (extra-tree), random forests, and support vector machines (SVM) to rank the feature importance for the seven Solar Orbiter SWA measurements in 2022, including proton speed and density made by PAS, and O^{7+}/O^{6+} , C^{6+}/C^{5+} , C^{6+}/C^{4+} , average charge state of $O(< Q >_{O})$,

and Fe/O density ratio made by HIS. Across the three models we tried, the ${\rm O^{7+}/O^{6+}}$ emerged as the most critical variable, followed by the $< Q>_O$ and proton speed. The Fe/O ratio turns out to be the least important feature compared to the other six, which is actually consistent with the study by Stakhiv et al. (2015, 2016) that shows the insensitivity of the Fe/O across intermediate and fast speed solar wind.

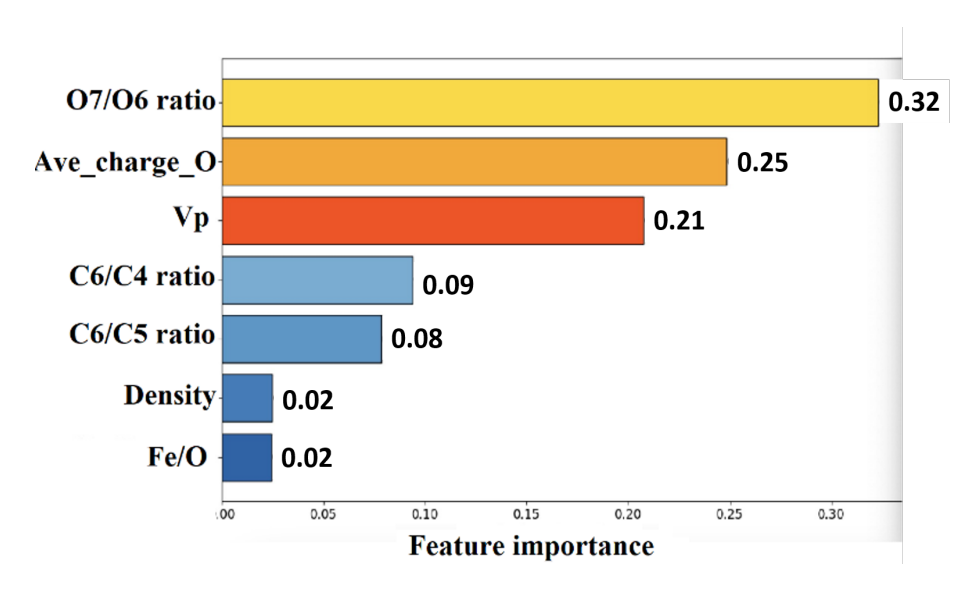


Fig. 5. Optimization of the solar wind in-situ SolO measurements by three ML algorithms (extra-tree, random forests, and SVM)

4 ML clustering and results

We proposed a self-supervised learning model, Solar-CDC, to handle high-performance unsupervised learning for solar wind data. It integrates the following basic ideas with a transformer for input data encoding.

Generate Pseudo Labels: Initially, the algorithm generates pseudo labels for the training data. These labels are based on the inherent structure and features of the data itself, rather than external annotations.

Use Pseudo Labels for Training: These pseudo labels are then used as if they were real labels to train a model. This step involves treating the pseudo-labeled data in a manner similar to a supervised learning problem, where the model learns to predict these labels.

Reassign Pseudo Labels: As the model learns and improves, the pseudo labels are periodically reassigned. This reassignment is based on the model's

evolving understanding of the data, ensuring that the labels remain relevant and accurate.

For pseudo-label generation, we used the K-Means algorithm. K-Means is a widely used partitioning method in data analysis for dividing a dataset into k distinct clusters based on similarity. K-Means is to minimize the following Within-Cluster Sum of Squares (WCSS)

WCSS =
$$\sum_{j=1}^{k} \sum_{x_i \in C_j} d(x_i, \mu_j)^2$$
, (1)

where C_i is the set of points in cluster i, and μ_i is the mean of points in C_i . The algorithm iteratively repeats the assignment and update steps until the centroids no longer change significantly, indicating that the algorithm has converged to a solution.

The proposed solar-CDC model then builds upon the fundamental learning principles with an emphasis on conducting clustering in the latent space generated by a transformer.

Encoder for Latent Representation: The process begins with an encoder, implemented as a transformer model in this study. It transforms the high-dimensional data into a lower-dimensional latent representation, capturing the essential characteristics of the data.

Cluster Latent Representation: The latent representation is then clustered using an unsupervised algorithm, grouping the data based on similarities identified in the latent space.

Creation of New Dataset with Pseudo Labels: The cluster assignments from the latent representation are used as new pseudo labels, effectively creating a new dataset where each data point is labeled based on its assigned cluster.

Addition of a Classification Head: A classification head is added to the encoder. This head is trained to predict the pseudo labels as if they were true labels, adhering to a supervised learning paradigm. This part of the process is known as the 'regular step'.

Transformer We briefly introduce the transformer as follows for the sake of understanding. The transformer encoder leverages self-attention to capture relationships in an input sequence, which is solar wind data in our study, with the following steps.

- 1. **Input Representation:** Let $\mathbf{X} \in \mathbb{R}^{n \times d}$ be the input matrix, where n is the sequence length and d is the dimensionality of each input vector.
 - 2. Multi-Head Self-Attention: Attention scores are computed as:

Attention(Q, K, V) = softmax
$$\left(\frac{\mathbf{Q}\mathbf{K}^{\top}}{\sqrt{d_k}}\right)\mathbf{V}$$
 (2)

with $\mathbf{Q} = \mathbf{X}\mathbf{W}_Q$, $\mathbf{K} = \mathbf{X}\mathbf{W}_K$, $\mathbf{V} = \mathbf{X}\mathbf{W}_V$, and multiple heads combined as:

$$MultiHead(\mathbf{Q}, \mathbf{K}, \mathbf{V}) = Concat(head_1, \dots, head_h)\mathbf{W}_O$$
 (3)

where each head $_i$ uses different learned projections.

3. Feed-Forward Network: Each position uses:

$$FFN(x) = \max(0, x\mathbf{W}_1 + b_1)\mathbf{W}_2 + b_2 \tag{4}$$

4. Layer Normalization and Residual Connections: Normalization and residual connections are applied as:

$$\mathbf{Z}_1 = \text{LayerNorm}(\mathbf{X} + \text{MultiHead}(\mathbf{Q}, \mathbf{K}, \mathbf{V}))$$
 (5)

$$\mathbf{Z}_2 = \text{LayerNorm}(\mathbf{Z}_1 + \text{FFN}(\mathbf{Z}_1)) \tag{6}$$

Stacking these layers allows the model to learn complex dependencies, useful for tasks like unsupervised learning for solar wind data to seek meaningful clustering in the proposed solar-CDC model.

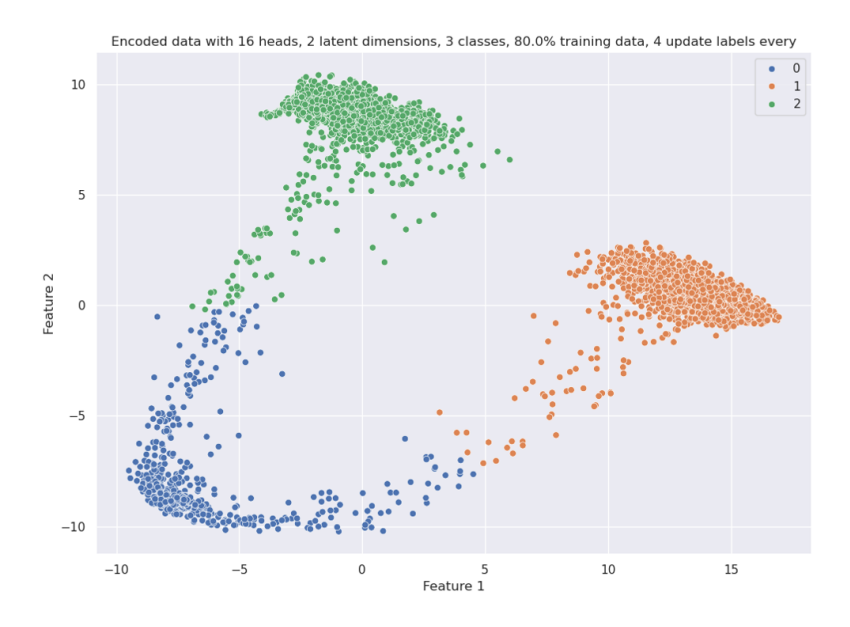


Fig. 6. The three clusters detected in the latent space by the encoder (transformer) from Solar-CDC.

5 Physical Properties of the Clusters

After the solar wind observations are clustered into different categories by the ML models, the physical properties (such as proton dynamic properties and heavy

ion compositions) of each cluster can be investigated and compared. Figure 7 summarize a comparison of these physical properties in the four clusters of solar wind as identified by the proposed Solar-CDC model. The observations shown in Figure 7 are 10-minute measurements made by Solar Orbiter/HIS and 10-minute averages of the 1.6-minute data made by PAS during 2022.

Figure 7a displays the comparison of the O^{7+}/O^{6+} and the proton speed; these two observables are in general anti-correlated when large ICMEs intervals are excluded. This anti-correlation has been empirically confirmed by decades of solar wind in-situ measurements, such as Ulysses [29], ACE [4], and Solar Orbiter; and also theoretically interpreted by the magnetic interchange reconnection for the solar wind plasma acceleration process in the corona (e.g. [30]). On the other hand, data analysis studies for the in-situ properties of the ICME plasma show that during long ICME intervals, the heavy ion charge state, such as O⁷⁺ (Richardson and Cane 2004) and Fe^{>16+} (Lepri et al. 2001) tend to be enhanced. Based on these statistical study, an empirical threshold using the O^{7+}/O^{6+} and proton speed to identify the ICME intervals is find (gold line in Figure 7a Richardson and Cane 2004). Data points that are above this threshold in 7a are likely to be ICME plasmas. The four clusters of the solar wind mostly still follow this anti-correlation, with some of the blue points (Cluster 2) are distributed above the gold line, which implies that some of the solar wind in Cluster 2 may be strongly suspected to be associated with ICMEs.

Figure 7b shows the histograms of O^{7+}/O^{6+} ratio in these four clusters. The most interesting feature of this plot is that Cluster 2 (blue) and Cluster 3 (black) are distinctly separated on either side of the vertical dotted line where $O^{7+}/O^{6+}=0.145$. This separating point of $O^{7+}/O^{6+}=0.145$ has been suggested by [4, 5] to distinguish the solar wind associated with coronal hole regions from those come from the outside of coronal holes, based on observations of ACE mission in the solar cycle 23, using traditional data analysis method. [11] employed a different set of data analysis focusing on analyzing the fast and slow wind interfaces, coincidentally, they also find that this $O^{7+}/O^{6+}=0.145$ is a separating points between the fast and slow streams. Note that these previous work do not use ML/AI technologies. In this work, we show that a clustering result provided by solar-CDC ML model strongly suggests that some very distinguishable groups of solar wind could be separated at $O^{7+}/O^{6+}=0.145$. The consistence of the results by the non-ML and ML analysis confirms: 1) the $O^{7+}/O^{6+}=0.145$ threshold is indeed a critical point, with the solar wind data on either side of this value exhibiting distinct physical features; 2) our ML model indeed uncovers some very essential features from the data that has physical magnificence.

Besides the very distinguished Cluster 2 and 3, Figure 7b also shows that a large (Cluster 1) that possesses about double of the data points as in Cluster 2, have a ${\rm O}^{7+}/{\rm O}^{6+}$ distribution in between of the Cluster 2 and 3, with a slight skew towards the lower value side, indicating that this cluster might be a combination of the both coronal-hole associated wind (as Cluster 2) and non-coronal-hole associated wind (as Cluster 3), and the current solar-CDC model did not categorize this Cluster 1 well. Also the Cluster 4 (red) which has the

minimum data points, has a wide spread of ${\rm O^{7+}/O^{6+}}$ value range, indicating that the solar-CDC model did not classify this type well.

Figure 7c represents the histograms of proton speed in the four clusters, and confirms with our understanding as learned from Figure 7b: Cluster 2 are non-coronal-hole associated slow speed solar wind (V< 450Km/s according to the blue histogram) and Cluster 3 is a coronal-hole-associated wind. However, we also notice that the proton speed distribution in Cluster 3 has two peaks, one is around the fast speed range (V $\sim 500Km/s$), and the other smaller one is around 400 Km/s. This bi-model speed feature of the coronal-hole-associated wind is exactly what we have found in previous study with ACE observations [4, 7]. The fast subgroup of the Cluster 3 might be associated to large coronal holes; and the slower subgroup might be associated with equatorial, small-sized and isolated coronal holes.

7d shows that the histograms of Fe/O abundance ratio in these four clusters are overlapped. This result is actually not very surprising. As reported by [8], Fe/O ratio could be vary similar in the coronal-hole and coronal-hole boundary associated wind, the only wind that has slightly enhanced Fe/O is the very slow, streamer associated wind in the equatorial region. The overlapping of the Fe/O histograms in these four clusters implies that our current ML model do not capture the streamer-associated high Fe/O ratio wind well. However, on the other hand, according to the feature selection result in Figure 5, Fe/O ratio is ranked the lowest importance, indicating that this parameter is not very efficient to be used to identify the features in the solar wind data. That could also be a reason why the outcome properties of Fe/O ratio in the four clusters are not distinguished well.

Figure 8 shows the physical properties of another clustering result using our solar-CDC deep clustering model on the extended Solar Orbiter dataset from Jan. 2022 to April 2023. The outcome is 3 clusters: Cluster 1 (red) possesses relatively low O^{7+}/O^{6+} ratio (Figure 8b), high proton speed (> 400 Km/s, 8c); Cluster 2 (black) has relatively high O^{7+}/O^{6+} ratio (Figure 8b) and slow proton speed (> 400 Km/s, 8c); and Cluster 3 (blue) is the hotest group with highest O^{7+}/O^{6+} ratio (Figure 8 a and b), however wide spread speed range. These features implies that Cluster 1 might be the coronal-hole associated fast wind; Cluster 2 is likely the non-coronal-hole, streamer-associated slow wind; and some of the Cluster 3 plasma could be ICMEs. The overlapping of the Fe/O histogram (Figure 8d) is again could be cause the nature of Fe/O itself that is not very effective to distinguish the types of solar wind, or could be attributed to the performance of our ML model.

The separation of Cluster 2 and 3 is at $O^{7+}/O^{6+}=0.12$ (dashed line in 8b), very close to the threshold we discussed in Figure 7b, ensuring the robustness of this separation point between different solar wind types.

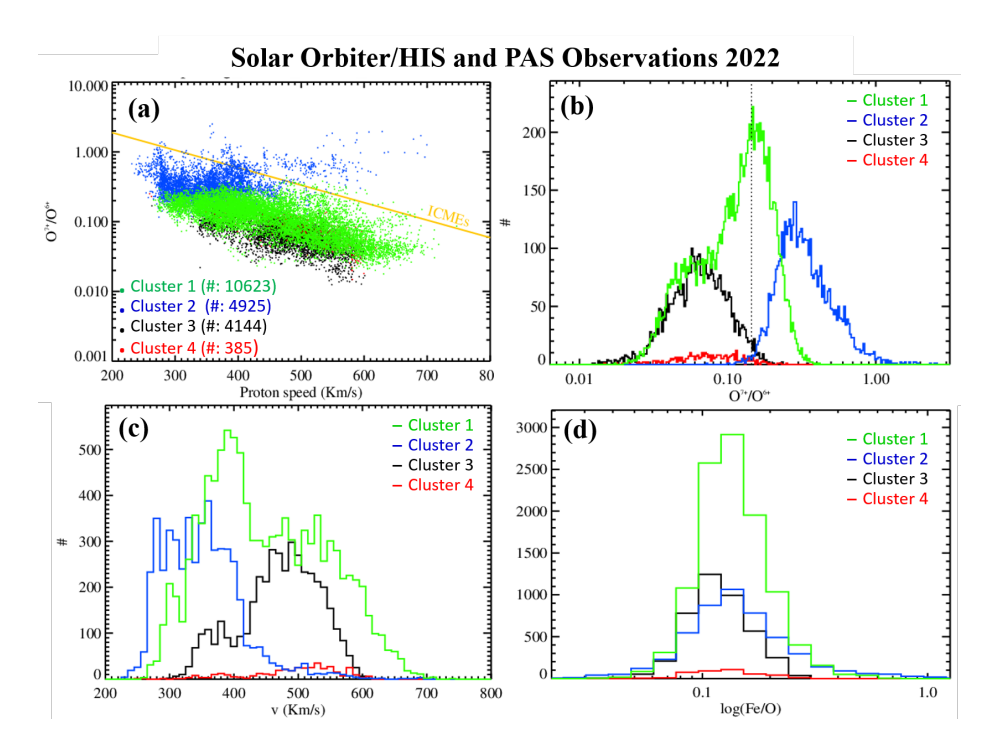


Fig. 7. Solar Orbiter HIS and PAS observations during the year of 2022. (a) Scattered plot of $\mathrm{O^{7+}/O^{6+}}$ versus $\mathrm{C^{6+}/C^{5+}}$ ratios. Four clusters are color coded in Green, blue, black and red with the numbers of the 10-minute data point labeled in the legend. Gold line is the ICME empirical threshold given by Richardson & Cane 2004. (b) Histograms of $\mathrm{O^{7+}/O^{6+}}$, (c) proton speed, and (d) Iron to Oxygen abundance ratio in the four clusters as identified by the Solar-CDC model. Vertical dotted line marks where $\mathrm{O^{7+}/O^{6+}}{=}0.145$.

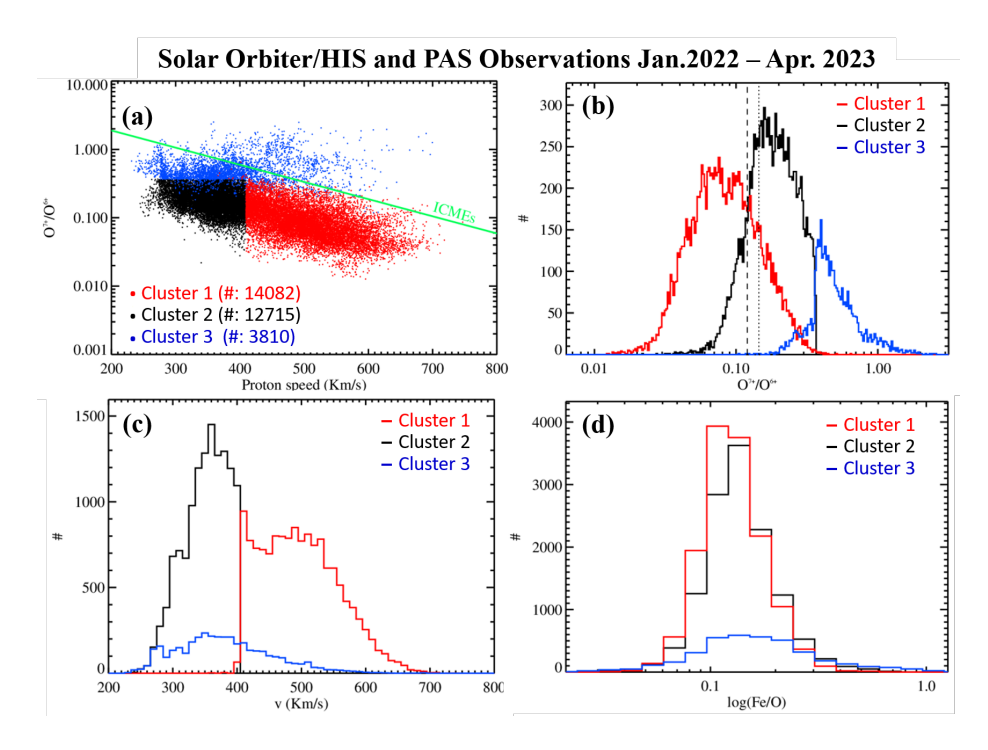


Fig. 8. Solar Orbiter HIS and PAS observations during January 2022 to April 2023. (a) Scattered plot of O^{7+}/O^{6+} versus C^{6+}/C^{5+} ratios. Three clusters are color coded in red, black, and blue with the numbers of the 10-minute data point labeled in the legend. Green line is the ICME empirical threshold given by Richardson & Cane 2004. (b) Histograms of O^{7+}/O^{6+} , (c) proton speed, and (d) Iron to Oxygen abundance ratio in the four clusters as identified by the Solar-CDC model. Vertical lines marks where O^{7+}/O^{6+} =0.145 (dotted), and 0.12.

6 Discussion and Conclusion

This coincidence of finding ${\rm O^{7+}/O^{6+}}{=}0.145$ as the separation point for coronal-hole and non-coronal-hole associated wind by our ML model indicates at least two benefits of using ML/AI to classify the solar wind types. 1) Due to their data-driven nature, ML/AI algorithms is a more objective and efficient approach to solar wind classification, while traditional methods often involve subjective or arbitrary decisions. Therefore, the result of ML/AI is closer to the nature of the data, with minimal human intervention. 2) Because of 1), ML/AI is excelled at extracting scientific insights from data more efficiently than traditional model-driven methods. Being adaptive and learning directly from data patterns make ML/AI more easily to unveil scientific characteristic hidden in the various solar wind datasets, especially extensively large ones, like Solar Orbiter.

The proposed Solar-CDC model demonstrates good latent meaningful clustering discovery capabilities. However, it sometimes exhibits overfitting by finding clusters limited to some important features such as velocity. It is possible that the transformer in the Solar-CDC does not capture the dynamics of solar wind time series data.

To improve the Solar-CDC model and address overfitting, we plan to enhance data representation by incorporating additional features, apply regularization techniques, adjust the model architecture by experimenting with hybrid models, fine-tune the attention mechanism, augment the training data, implement time series-specific techniques, optimize hyperparameters, use cross-validation, and post-process clusters based on domain knowledge. These steps will help the model capture the complex dynamics of solar wind data and reduce overfitting, leading to more accurate and generalizable clustering results.

Acknowledgements

L.Z. is supported by NASA Grants 80NSSC21K0579, 80NSSC22K1015, NSF SHINE grant 2229138, and NSF Early Career grant 2237435. H.H is supported by the McCollum endowed chair startup fund of Baylor University.

References

- S. P. Owocki, T. E. Holzer, and A. J. Hundhausen, The Solar Wind Ionization State as a Coronal Temperature Diagnostic, Astrophys. J., 275, 354-366, 1983
- Ko, Yuan-Kuen, Raymond, J. C., Zurbuchen, T. H., Riley, P., Raines, J. M., and Strachan, L. Abundance Variation at the Vicinity of an Active Region and the Coronal Origin of the Solar Solar Wind, ApJ, 646 2, 1275-1287, 2006
- 3. Liu, S., and Su, J. T., Multi-Channel Observations of Plasma Outflows and the Associated Small-Scale Magnetic Field Cancellations on the Edges of an Active Region, Astrophysics and Space Science, 351, 2, 417-425, 2014
- 4. Zhao, L., T. H. Zurbuchen, and L. A. Fisk, Global Distribution of the Solar Wind during Solar Cycle 23: ACE Observations, Geophys. Res. Lett., 36, L14104, 2009

- Zhao, L., E. Landi, T. H. Zurbuchen, L. A. Fisk and S. T. Lepri, The Evolution of 1 AU Equatorial Solar Wind and its Association with the Morphology of the Heliospheric Current Sheet from Solar Cycles 23 to 24, The Astrophysical Journal, 793, 44, 8pp., doi: 10.1088/0004-637X/793/1/44, 2014
- Zhao, L., S. E. Gibson, and L. A. Fisk, Association of Solar Wind Proton Flux Extremes with Pseudostreamers, J. Geophys. Res. Space Physics, 118, 2834-2841, 2013a
- Zhao, L., Landi, E., Lepri, S.T., Gilbert, J.A., Zurbuchen, T.H., Fisk, L.A., Raines, J.M.: On the Relation Between the In-Situ Properties and the Coronal Sources of the Solar Wind. Astrophys. J. 846(2)(135) (2017)
- 8. Stakhiv, M., Landi, E., Lepri, S. T., Oran, R., & Zurbuchen, T. H., On The Origin Of Mid-Latitude Fast Wind: Challenging The Two-State Solar Wind Paradigm, 2015, The Astrophysical Journal, 801, 100
- M. Stakhiv, S. T. Lepri, E. Landi, P. Tracy, and T. H. Zurbuchen, On Solar Wind Origin and Acceleration: Measurements from ACE, Astrophys. J., 829, 2, 117, 2016
- 10. Owens, M.J., N. U. Crooker, & M. Lockwood, Solar cycle evolution of dipolar and pseudostreamer belts and their relation to the slow solar wind, J. Geophys. Res. Space Physics, 119, doi:10.1002/2013JA019412, 2014
- Crooker, N. U., & R. L. McPherron, Coincidence of composition and speed boundaries of the slow solar wind, Astrophys. J., 117, A09104, 2012
- 12. A. J. Hundhausen, 1977, An interplanetary view of coronal holes, in Coronal Holes and High Speed Wind Streams, p. 225-329
- Y.-M. Wang, N. R. Sheeley, Jr. & N. B. Rich, Coronal Pseudostreamer, 2007 ApJ 658 1340
- Abramenko, V., Yurchyshyn, V., Linker, J., Mikić, Z., Luhmann, J. And Lee, C.,
 Low- Latitude Coronal Holes at the Minimum of the 23rd Solar Cycle, ApJ, 712, 2,
 813 818, 2010
- de Toma, G., Gibson, S. E., Emery, B. A., and Arge, C. N. Evolution of Coronal Holes and Implications for High-Speed Solar Wind During the Minimum Between Cycles 23 and 24, SOHO–23 proceeding, 217, 2010
- Zhao, L., S. E. Gibson, and L. A. Fisk, Association of Solar Wind Proton Flux Extremes with Pseudostreamers, J. Geophys. Res. Space Physics, 118, 2834-2841, 2013a
- L. Zhao, E. Landi, L. A. Fisk, and S. T. Lepri, The Coherent Relation Between the Solar Wind Proton and Speed and O7+/O6+ Ratio and its Coronal Sources, AIP Conference Proceedings, 1720, 020007, 2016a
- R. von Steiger, & Zurbuchen, T. H., Polar coronal holes during the past solar cycle: Ulysses observations, J. of Geophys. Res. (Space Physics), 116, A01105, 2011
- Geiss, J. Constraints on the FIP mechanisms from solar wind abundance data,
 Space Sci. Rev. 85 (1-2), 241-252, doi: 10.1023/A:1005198416520, 1998
- 20. N. A. Schwadron, L. A. Fisk, & T. H. Zurbuchen, Elemental Fractionation in the Slow Solar Wind, Astrophys. J., 521, 2, p. 859-867, doi: 10.1086/307575, 1999
- Von Steiger, R., Schwadron, N.A., Fisk, L.A., Geiss, J., Gloeckler, G., Hefti, S., Wilken, B., Wimmer-Schweingruber, R., Zurbuchen, T.: Composition of Quasi-Stationary Solar Wind Flows from Ulysses/Solar Wind Ion Composition Spectrometer. Journal of Geophysical Research. 105(27217-27238) (2000) DOI: 10.1029/1999JA000358.
- 22. R. von Steiger, & T. H. Zurbuchen, Solar Metallicity Derived From In-situ Solar Wind Composition, Astrophys. J., 816, 13, 2016

- Landi, E., Gruesbeck, J.R., Lepri, S.T., Zurbuchen, T. H. & Fisk, L. A., Charge State Evolution in the Solar Wind. II. Plasma Charge State Composition in the Inner Corona and Accelerating Fast Solar Wind, 2012 Astrophys. J., 761, 48
- Lepri, S. T., Zurbuchen, T. H., Fisk, L. A., Richardson I. G., Cane, H. V., & Gloeckler, G., Iron charge distribution as an identifier of interplanetary coronal mass ejections, J. of Geophys. Res., vol. 106, No. A12, Pages 29,231-29,238, December, 1, 2001
- 25. S. T. Lepri and T. H. Zurbuchen, DIRECT OBSERVATIONAL EVIDENCE OF FILAMENT MATERIAL WITHIN INTERPLANETARY CORONAL MASS EJECTIONS, 2010 ApJL 723 L22
- 26. Müller, D., St. Cyr, O. C., Zouganelis, I., et al., The Solar Orbiter mission Science overview, A&A, 642, A1, doi: 10.1051/0004-6361/202038467, 2020
- Owen, C. J., Bruno, R., Livi, S., et al., The Solar Orbiter Solar Wind Analyser (SWA) suite, A&A, 642, A16, doi: 10.1051/0004-6361/201937259, 2020
- Livi, S., Lepri, S. T., Raines, J. M., et al. First results from the Solar Orbiter Heavy Ion Sensor, A&A, 676, A36, doi: 10.1051/0004-6361/202346304, 2023
- G. Gloeckler, T. H. Zurbuchen, and J. Geiss, Implications of the observed anticorrelation between solar wind speed and coronal electron temperature, J. Geophys. Res., 108, CideID 1158, 2003
- L. A. Fisk, Acceleration of the Solar Wind as a Result of the Reconnection of Open Magnetic Flux With Coronal Loops, J. Geophys. Res., 108, 1157, 2003
- 31. J. M. Laming, The FIP and Inverse FIP Effects in Solar and Stellar Coronae, Living Reviews in Solar Physics, vol. 12, issue 1, article id. 2, 76 pp.